Triggering effects of large topography and boundary layer turbulence on convection over the Tibetan Plateau

Xiangde Xu[1], Yi Tang[1,2], Yinjun Wang[1], Hongshen Zhang[3], Ruixia Liu[4] and Mingyu Zhou[5]

[1] State Key Laboratory of Severe Weather, Chinese Academy of Meteorological Sciences, Beijing, China.

[2] School of Environmental Studies, China University of Geosciences, Wuhan, China.

[3] Peking University, Beijing, China

[4] CMA Earth System Modeling and Prediction Centre (CEMC), Beijing, China

[5] National Marine Environmental Forecasting Center, Beijing, China

Corresponding author: Yinjun Wang (pbl_wyj@sina.cn) and Hongshen Zhang (hsdq@pku.edu.cn)

Abstract

In this study, we analyze the diurnal variations and formation mechanism of low clouds at different elevations. We further discuss whether there exists triggering mechanism for convection over the Tibetan Plateau (TP), and whether there is an association among low air density, strong turbulence and ubiquitous "popcorn-like" cumulus clouds. The buoyancy term (BT) and shear term (ST) over the TP are significantly greater than those at the low elevation, which is favorable for the formation of increasing planetary boundary layer height (PBLH), and also plays a key role in the convective activities in the lower troposphere. ~~The lifting condensation level (LCL) increases with the increasing of PBLH-LCL over the TP.~~ From the viewpoint of global effects, the triggering of convection by boundary layer dynamics is analyzed over TP but also in the Northern Hemisphere over the Rocky Mountains. It is found that ST and BT are strong over both high elevation regions.~~the triggering effects of the dynamical structure within the boundary layer on convective clouds in the Northern Hemisphere are analyzed. There are strong ST and BT at two high elevation regions (TP and Rocky Mountains), and t~~ The strong thermal turbulence and large scale ascending motion jointly results in obvious positive value of PBLH-LCL ~~at high elevation regions~~ under low ~~RH~~ relative humidity (RH) condition over the TP. ~~in the Northern Hemisphere. The values of PBLH LCL slightly greater than zero correspond spatially to increased low cloud cover (LCC) in the central part of Rocky Mountains, but the obvious large-scale subsidence on both sides of the mountain leads to strong inversion above PBL and lower RH in PBL, which further lead to decreased LCC in these areas. Thus less LCC is generated at Rocky Mountains compared to the~~

TP. The obvious large-scale subsidence on both sides of the Rocky Mountain especially the western side leads to inversion above PBL and lower RH within the PBL, which further lead to negative value of PBLH-LCL and decreased low cloud cover (LCC) in most part of Rocky Mountain. The slightly greater than zero PBLH-LCL corresponds spatially to increased LCC in the partial regions of central Rocky Mountain. Thus less LCC is generated at the Rocky Mountains compared to the TP.

Introduction

The Tibetan Plateau (TP), which resembles a "third pole" and a "world water tower", plays an important and special role in the global climate and energy–water cycle (Xu et al., 2008; Wu et al., 2015). The TP covers a quarter of China. Additionally, the average altitude of the TP is 4000 meters, reaching 1/3 of the tropopause height, so it is called the "World Roof". Cumulus convection over the TP transfers heat, moisture and momentum into the free troposphere, which can impact the atmospheric circulation regionally and globally (Li and Zhang, 2016; Xu et al., 2014) and reveals the important "window effect" for the transfer and exchange of global energy and water vapor over the TP. It is the a dynamic effect from caused by the special heat source that constitutes the "window effect" and "thermally driven" mechanism over the TP.

The results of the second Tibetan Plateau Experiments (TIPEX II), which were carried out in 1998, show that the strong convective plumes within PBL observed by sodar and a frequently occurred deep mixed layer (>2 km) can lead to ubiquitous "popcorn-like" cumulus clouds in Dangxiong, as proposed by Zhou et al. (2000), and Xu et al. (2002) came up with a comprehensive physical pattern of land-air dynamic and thermal structure on the TP (Xu et al., 2002; Zhou, 2000). The previous studies have done many valuable researches on the triggering mechanism of moist convection over moist and dry surfaces based on atmospheric observations and simulations (Ek and Mahrt, 1994; Findell and Eltahir, 2003; Gentine et al., 2013). For dry surface, the weak stratification and strong sensible heat flux result in the rapid growth of PBLH so that the relative humidity at the top of the boundary layer RH_{top} increases rapidly, which favors the formation of clouds. For moist surface, strong stratification and evaporation (small bowen ratio) not only cause slow growth of PBLH but also increase the mixed layer specific humidity and RH_{top}, which favor the formation and development of clouds. Taylor et al. (2012) found that the afternoon rain falls preferentially over soils that are relatively dry compared to the surrounding area, especially for semi-arid regions. Guillod et al. (2015) reconciled spatial and temporal soil moisture effects on the afternoon rainfall. They showed that afternoon precipitation events tend to occur during wet and heterogeneous soil moisture conditions, while being located over comparatively drier patches. Tuttle et al. (2016) showed the empirical evidence of contrasting soil moisture–precipitation feedbacks across the United States, and they found that soil moisture anomalies significantly

influence rainfall probabilities over 38% of the area with a median factor of 13%. Findell et al. (2003) analyzed the model results over dry and wet soils in Illinois. They summarized the predictive capability of rain and shallow clouds by using the convective triggering potential (CTP) and a low-level humidity index, with HI_{low} as measures of the early morning atmospheric setting. Our previous studies pointed out that the developments of these cumulus clouds are related to the special large scale dynamic structure and turbulence within PBL over the TP (Xu et al., 2014; Wang et al., 2020). In addition, Wang et al., (2020) pointed out that, despite the same relative humidity between eastern China and the TP, the lower temperature over the TP results in a lower lifting condensation level. With the same surface sensible heat flux, lower air density over the TP results in a larger buoyancy flux and a deeper boundary layer. All the above results indicate the topography of the TP plays a major role in increasing the occurrence frequency of strong convective clouds (Luo et al., 2011). This conclusion is consistent with the viewpoint of Flohn (1967) who emphasized the chimney effect of the huge cumulonimbus clouds on heat transfer in the upper troposphere.

The TP is one of the regions in China that is featured with high frequency of cumulus clouds, and the development of a cumulus system is related to both the turbulence and special dynamical structure in the PBL over the TP. The vertical motion over the TP is associated with anomalous convective activities. However, as Li and Zhang (2016) mentioned, the details of PBL processes are not very clear. The same is true for the diurnal variations and formation mechanism of low clouds over the TP and low elevation regions. The different variation characteristics of these low clouds at different elevations and regions also need to be discussed and analyzed. Moreover, we need to investigate whether there exists "high efficiency" triggering mechanisms for convection over the TP, and whether there is an association among low air density, strong turbulence and ubiquitous "popcorn-like" cumulus clouds. Is there also strong turbulence at higher elevation regions with lower air density in the globe? What is the impact of the large scale vertical motions on clouds? Because both the TP and Rocky Mountains are high elevation regions covering large mid-latitude areas, we select these two typical regions to make a deep analysis. Unlike our previous paper by Wang et al. (2020), in this study we mainly focus on the comparison between these two regions to analyze the above scientific questions.

2 Observational and reanalysis data

We use in situ measurements of temperature (T) and relative humidity (RH) at 2 m height, surface pressure data every hour, and low cloud cover (LCC) every three hours from 2402 automatic weather stations from June to August of 2010-2019 in China. LCC here refers to the fraction of the sky covered by low clouds as estimated by human observers, including five cloud types: nimbostratus (Ns), stratocumulus (Sc), stratus (St), cumulus (Cu), and deep convection (DC). These surface observation datasets are provided by China National Meteorological Information Center.

In addition, we use the hourly 0.25° x 0.25° ERA5 reanalysis surface-layer data in summer (June 1 to August 31) from 2010 to 2019 (Hersbach et al., 2020).

We use more than 4 years (from June 15 2006 to August 31 2010) of the satellite (CloudSat radar and Calipso lidar)-merged cloud classification product 2B-CLDCLASS-lidar to calculate the mean LCC with 1°x1° resolution at about 2:00 pm and 2:00 am LT in summer. The introduction of this product and details of the LCC calculation methods are summarized in Sassen and Wang (2008) and Wang et al (2020).

We use a Gaofen 4 (GF 4) visible satellite image with ~~the~~ a spatial resolution of 50 m on August 4 of 2020 to show the organized structures (cellular convection) in southeastern TP, as shown in Figure 1. GF 4 is a geostationary earth observation satellite in the Gaofen series of Chinese civilian remote sensing satellites. We also use the 1 year (from June 1 to August 31 of 2016) geostationary satellite ~~himawari~~Himawari-8 retrieval product (cloud top height) over land in East Asia.

In this study, we also use temperature (T) at 2 m height, relative humidity (RH) at 2 m height, surface pressure and planetary boundary layer height (PBLH) from ERA5 reanalysis data from 2010 to 2019. To be specific, the above four variables represent hourly average~~d~~ values for each month (24 values in total for a month). The lifting condensation level (LCL) is calculated by the method proposed by (Romps, 2017).

Using sensible heat flux H, Northward turbulent surface stress τ_y and Eastward turbulent surface stress τ_x from ERA5 reanalysis data, we calculate the buoyancy term (BT) ($g/\theta_v \; \overline{w'\theta_v'}$) and shear term (ST) ($-\partial\bar{u}/\partial z \, \overline{u'w'}$) in the TKE equation for each grid. Both of these two terms can be used to analyze the effect of boundary layer turbulence in surface layer on convection. The details of the method for computing BT and ST are as follows:

The shear term (ST) ($-\partial\bar{u}/\partial z \, \overline{u'w'}$ ~~$=\partial\bar{u}/\partial z\,\overline{u'w'}-\partial\bar{v}/\partial z\,\overline{v'w'}$~~) and buoyancy term (BT) ($g/\theta_v \; \overline{w'\theta_v'}$) in the TKE equation maintain the turbulent motions. In order to simplify calculations, the x-axis is directed along the average wind. Assuming horizontal homogeneity and no mean divergence, the TKE equation is written as

$$\frac{\partial \bar{e}}{\partial t} = \frac{g}{\theta_v}\overline{w'\theta_v'} - \overline{u'w'}\frac{\partial \bar{u}}{\partial z} - \frac{\partial\left(\overline{w'e}\right)}{\partial z} - \frac{1}{\bar{\rho}}\frac{\partial\left(\overline{w'p'}\right)}{\partial z} - \varepsilon. \tag{1}$$

The left side of eq. (1) is the local time variation $\partial\bar{e}/\partial t$, and the terms on the right-hand side of eq. (1) describe the buoyancy and shear energy production or consumption, turbulent transport of $\bar{e}$, pressure correlation and viscous dissipation (Stull, 1988).

Here we use eq. (2) to calculate the virtual potential temperature θ_v, and $\overline{w'\theta_v'}$ is derived from eq. (3). Finally, we derive BT.

$$\theta_v = T\left(1+0.608q\right)\left(\frac{p_0}{p}\right)^{\frac{R}{c_p}}, \tag{2}$$

$$H = \rho c_p \, \overline{w'\theta_v'}, \tag{3}$$

159   Where g = 9.8 m s^{-2} is the gravitational constant, and H (W m^{-2}) is the sensible
160 heat flux, ρ (kg m^{-3}) is the air density, R is the specific gas constant for dry air, c$_p$
161 (=1004 J kg^{-1} K^{-1}) is the specific heat of air at constant pressure, T is the air
162 temperature at 2 m height, q is the specific humidity at 2 m height, p_0 and p are
163 standard atmospheric pressure and surface pressure, respectively.

164   The wind shear is determined from heat flux H and momentum flux τ obtained
165 from the ERA5 reanalysis data. Because we cannot directly obtain the τ from ERA5
166 product list, we need to use eq. (4) to calculate τ.

167 $$\tau = \sqrt{\tau_x^2 + \tau_y^2}, \tag{4}$$

168   According to Monin Obukhov similarity theory wind shear is given as

169 $$\frac{\partial \overline{u}}{\partial z} = \phi_m(\zeta)\frac{u_*}{\kappa z}, \tag{5}$$

170   Where ϕ_m is the Monin Obukhov stability function for momentum, $u_*^2 = \tau/\rho$.
171 The von Karman constant κ =0.4, $\overline{u}$ is the horizontal wind speed in the surface
172 layer.

173     $\zeta = z/L$ with z = height and L = Obukhov stability length defined as in Gryanik et
174 al. (2020) as

175 $$\zeta = \frac{z}{L}, L = -\frac{(\tau/\rho)^{3/2}}{\kappa(g/\theta_v)(H/\rho c_p)}. \tag{6}$$

176   ϕ_m is the Monin Obukhov stability function, here we use eq. (7) and eq. (8) for
177 stable and unstable conditions to derive ϕ_m (Dyer, 1974),

178 $$\phi_m = 1 + 5\zeta, (\zeta > 0) \tag{7}$$
179 $$\phi_m = (1-16\zeta)^{-1/4}, (\zeta < 0) \tag{8}$$
180   Then we use eq. (9) to derive $-\overline{u'w'}$. Finally, we derive ST.
181 $$\overline{u'w'} = -\tau/\rho. \tag{9}$$

182 For ERA5 reanalyze data, the $\partial\overline{u}/\partial z$ in the surface layer is estimated as

183 $$-\frac{\partial \overline{u}}{\partial z} = \phi_m(\zeta)\frac{u_*}{kz}, \tag{4}$$

184 (i) Unstable conditions $(\zeta = z/L < 0)$. The non-dimensional wind profiles ϕ_m are

185 deduced from eq.(5), as proposed by (Dyer, 1974):

186 $$\phi_m = (1-16\zeta)^{-1/4}, (\zeta < 0) \tag{5}$$

187 (ii) Stable conditions $(\zeta = z/L > 0)$. The stable profile functions are assumed to have

188 the empirical forms proposed by Holtslag and Bruin (1988). The universal profile

189 stability function ψ_m can be written as

$$\psi_m = -b\left(\zeta - \frac{c}{d}\right)\exp(-d\zeta) - a\zeta - \frac{bc}{d}, \tag{6}$$

Where a = 1, b = 2=3, c = 5, and d = 0.35. Then ϕ_m can be estimated with the

help of the relationship $\phi_m = 1 - \zeta\left(\partial\psi_m/\partial\zeta\right)$.

$$\zeta = \frac{z}{L}, L = -\frac{(\tau/\rho)^{3/2}}{\kappa(g/\theta_v)(H/\rho c_p)}, \tag{7}$$

$$\tau = \sqrt{\tau_x^2 + \tau_y^2}, \tag{8}$$

$$\tau = \rho u_*^2, \tag{9}$$

$$\tau = -\rho\overline{u'w'}. \tag{10}$$

Where the von Karman constant $\kappa = 0.4$, and $z = 10$ m. $\overline{u}$ is the horizontal wind speed at level z and u_* is the frictional velocity. The stability parameter z/L is defined, and the Obukhov length L can be directly written as a function of τ and H in eq.(7) (Gryanik et al. 2020). τ_x and τ_y are the Eastward and Northward turbulent surface stress, respectively. τ is turbulent fluxes of momentum, which can be calculated by using eq. (8). Then we use eq. (9) to derive u_*. We also use eq. (10) to derive $-\overline{u'w'}$. Finally, we derive ST.

3 Results

Figure 2 shows the spatial distribution of over-land low cloud cover (LCC) in China from June to August of 1951-2019. Compared to the low LCC in eastern China, the high value areas of LCC are mainly located in the mid-eastern TP and the area of the upper Yangtze River Valley. But low LCC is also identified in western and northern parts of TP. We will make a further discuss about it in subsequent paragraphs. Using four years of CloudSat-Calipso satellite data, Li and Zhang (2016) confirmed that the climatological occurrence of cumulus over the TP is significantly greater than that in mid-eastern China on the same latitude. The elevated land surface with strong radiative heating makes the massive TP a favorable region for initiating convective cells with a high frequency of cumulonimbus and mesoscale convective systems (Sugimoto and Ueno, 2012). As a strong heat source, the TP has frequent convective activities in summer. During the TIPEX Ⅱ in 1998, the long and narrow thermal plume corresponding with vigorous cellular convection on micro-scale was observed by sodar in Dangxiong. As shown in Figure 1, the shallow convective clouds on a horizontal scale from hundreds of meters to several kilometres over the southeastern TP (92.7-96.2E, 29.5-31.3N) are probably related to the organized eddies on the

222 meso-scale and micro-scale over the TP. The cloud fraction over the southeastern TP
223 is about 31.3%.

224   As shown in Figure 3, in general, LCC increases with ~~the~~ increasing elevation.
225 The median of LCC_H is significantly greater than those of LCC_L and LCC_M
226 throughout the day. The diurnal variations of LCC_L and LCC_M are generally
227 distributed in unimodal pattern, with the maximum appearing at 2:00 pm ~~BT~~ Beijing
228 time (median LCC_L = 37%, LCC_M = 38%) and low values (~20%) are maintained
229 during the night. The diurnal variation of LCC_H presents a bimodal curve with the
230 maximum appearing at 5:00 pm ~~BT~~ Beijing time (median LCC_H = 69%) and the
231 secondary local maximum appearing at 8:00 am Beijing time~~BT~~ (median LCC_H =
232 61%). Compared to the low elevation, the interquartile ranges (IQRs) of LCC_H are
233 smaller than those of LCC_L and LCC_M, which imply the LCC_H maintains high values
234 during the day. To further confirm and compare the above results with in situ
235 measurements, using ERA5 LCC data, we also add Figure S1 to show the diurnal
236 cycle of LCC in summer in East Asia and North America in the supplementary
237 material.
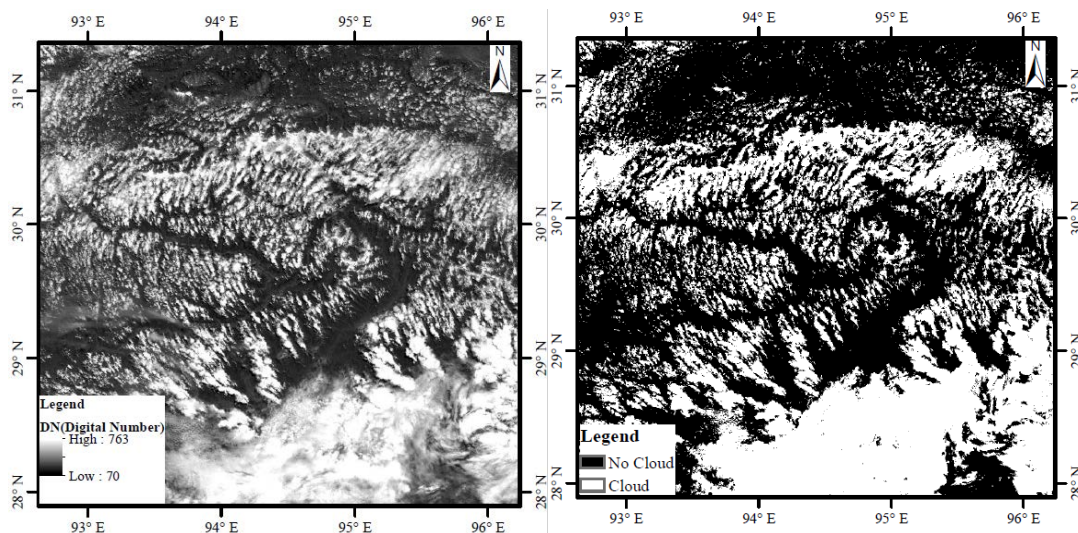
238
239   Figure 1. The (a) digital number (DN) and (b) spatial distribution of cloud in
240 southeastern TP from geostationary earth observation satellite Gaofen 4 (GF4) at
241 12:00 pm Beijing time (about 10:20 am local time) on August 4 of 2020. Here we
242 simply use DN = 250 as a threshold. All the grids in Figure (a) are divided into two
243 classes (DN > 250, cloud; DN < 250, no cloud), and then we give Figure (b).
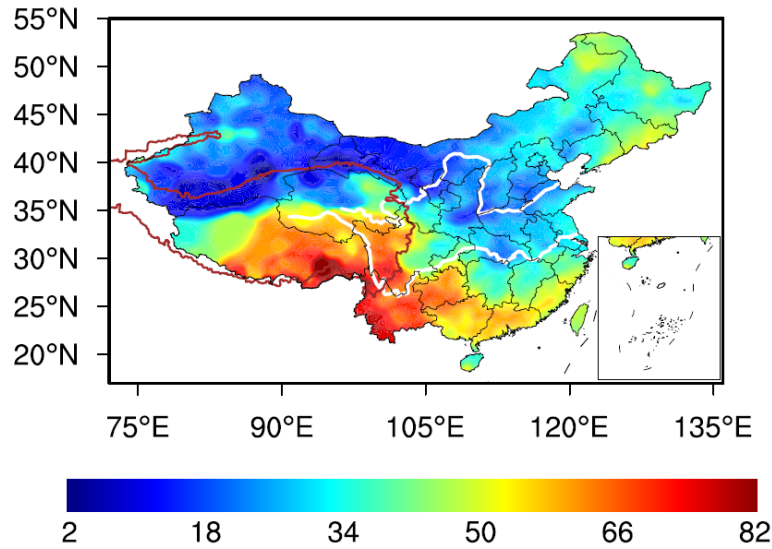
Figure 2. The summer mean LCC derived from surface observations from 1951 to 2019 in China. The thick red contour denotes the 2.5 km topography height referred to as the TP. The white lines located in northern and southern parts of China denote the Yellow and Yangtze River, respectively.
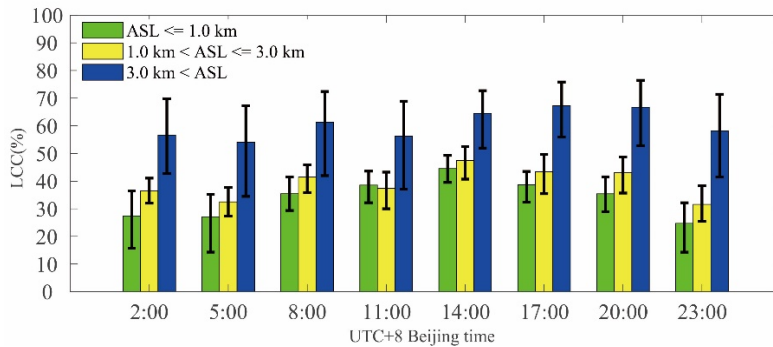
Figure 3. The diurnal cycle of LCC in summer from 2010 to 2019 at different altitudes above sea level (ASL): ASL ≤ 1.0 km (LCC$_L$), 1.0 km < ASL ≤ 3.0 km (LCC$_M$), and 3.0 km < ASL (LCC$_H$). It should be noted that all the sites are ranged from 27N to 40N in China, and each sample is derived from monthly mean LCC at a particular time in summer for each site. The bar and error bar represent the median values and interquartile ranges (IQRs) of LCC, respectively. The subscripts L, M and H of LCC denote the low, mediun and high clouds, respectively.

260

261

262

263
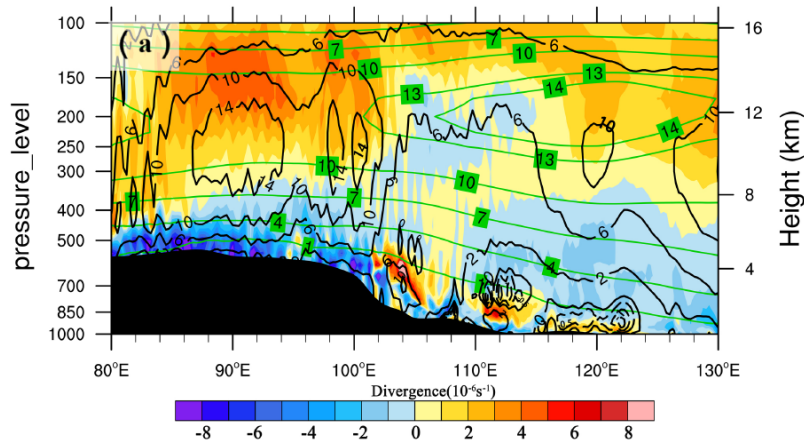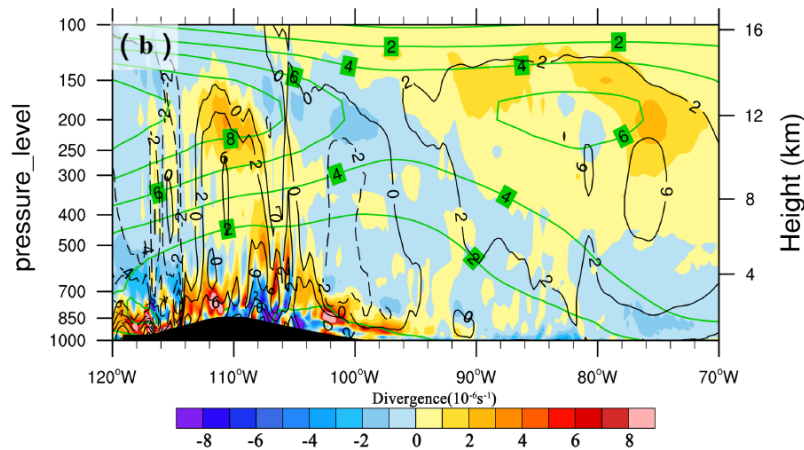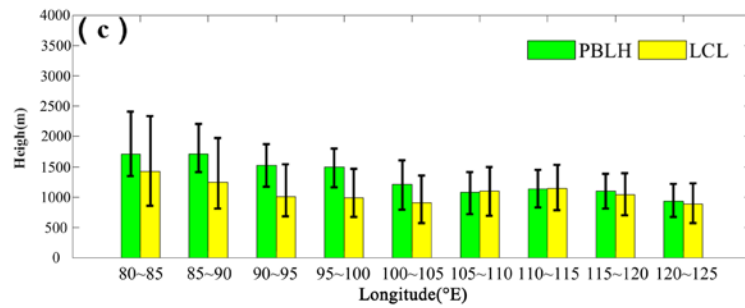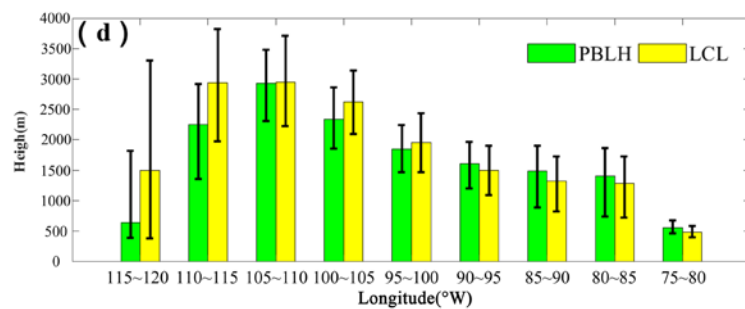
Figure 4. Vertical distribution of <u>summer mean</u> divergence ($\underline{10^{-6}}$ s^{-1}) (shaded) <u>at 2:00 pm local time from 2010 to 2019</u> at the latitude across sections from 30N to 35N in (a) East Asia and (b) North America. The green and black contours denote the summer mean U- (m s^{-1}) and W- (10^{-2} m s^{-1}) wind components ~~at local time 2:00 pm from 2010 to 2019 along 30N~35N~~ with the zonal circulations, respectively. The solid and dash<u>ed</u> contour lines represent the positive and negative values, respectively. The

black shaded areas represent topography. Figure (c) and (d) are Tthe PBLH (green) and LCL (yellow) versus longitude in (c) East Asia and (d) North America, respectively. The bar and error bar represent the median values and interquartile ranges (IQRs), respectively.
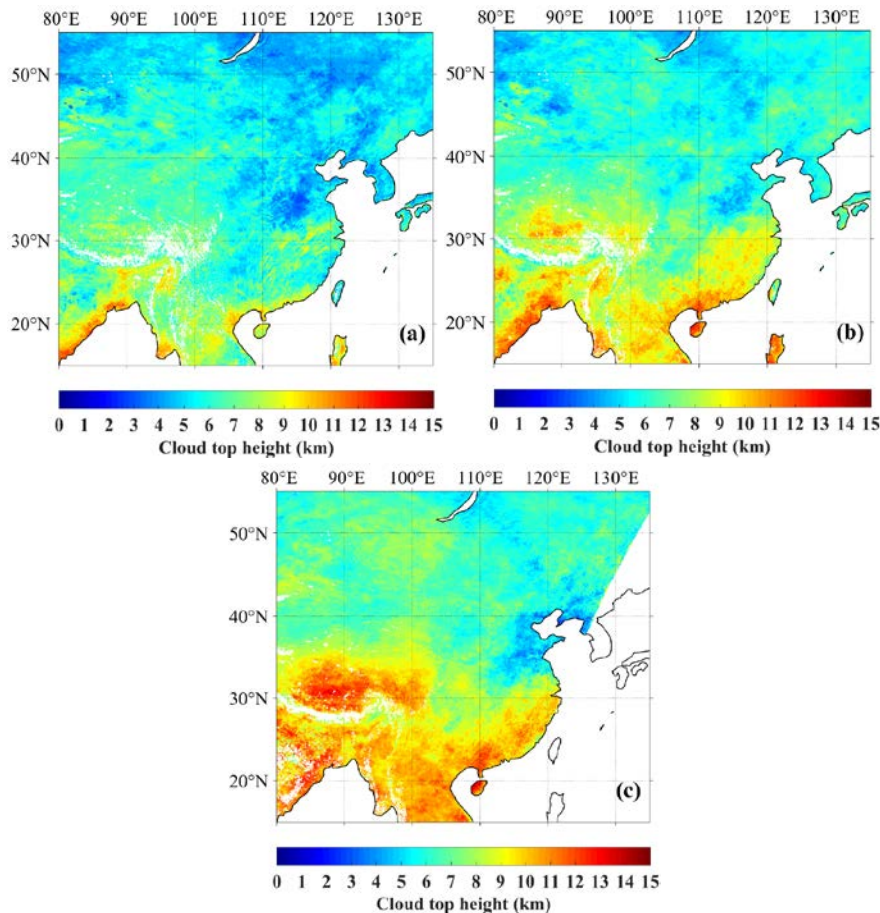
Figure 5. The median cloud top height derived from the himawariHimawari-8 retrieval product at three Beijing times: (a) 2:30 pm±0.5h (b) 4:30 pm±0.5h (c) 6:30 pm±0.5h from June to August in 2016 over land in East Asia. Missing data are shaded in white color.

On the other hand, we note that, compared to eastern China, there is no obvious decrease trend of decreasingfor the LCC over the TP from late afternoon to evening as shown in Figure 3. Based on the spatial distribution of topography in the Northern Hemisphere as shown in Figure 7 (a), it is clear that both the TP (27-40N, 70-105E) and Rocky Mountains (27-40N, 103-120W) in North America are two large areas with high elevations in mid-latitude regions in the Northern Hemisphere, so here we select these two typical large topography regions to analyze the triggering effects of large topography and related dynamical structure within the boundary layer on convective clouds. As shown in Figure 4 (a), In in general, there are obvious large scale ascending motions from middle troposphere (~500 hPa)near surface layer to upper troposphere (~200 hPa) over the TP, which correspond with the convergence at 500 hPa and the divergence at 200 hPa. The convergence in the middle troposphere (the blue shaded areas) and the divergence in the upper troposphere (the orange

shaded areas) are usually associated with the deep convection over the TP, ~~as shown in Figure 4 (a)~~. Figure 4 (c) shows there are generally positive PBLH-LCL (~500 m) over the TP, and the median and IQR of PBLH are close to those of LCL in East ~~Asia~~China. These results are consistent with the conclusions proposed by Xu et al. (2014) and Wang et al. (2020). In contrast, Figure 4 (b) shows there are only weak large scale ascending motions from near surface layer to the middle troposphere over the Rocky Mountains~~., and T~~the large-scale subsidence on both sides of the Rocky Mountains especially the western side can lead to ~~strong~~ inversion above PBL and lower RH ~~in near surface layer~~within the PBL, which can be verified by the vertical distribution of the dθ_v/dz and RH at the latitude across sections from 30N to 35N over the Rocky Mountains in Figure S2. There exists a high value center of dθ_v/dz at about 950 hPa (or 850 hPa) on western (or eastern) side of the Rocky Mountains, and the RH within the PBL is generally less than 55%. The former restricts the growth of PBLH during the day, while the latter leads to ~~the~~ an increased LCL. Thus, negative PBLH-LCL is identified on both sides of the Rocky Mountains (30-35N, 110-120W and 30-35N, 100-105W), especially for the western Rocky Mountain (30-35N, 110-120W) with strong large-scale subsidence, as shown in Figure 4 (d).Dynamic processes of vapor transport are generated because of the thermal structure of the TP, which is similar to the conditional instability of the second kind (CISK) mechanism of tropical cyclones (Smith, 1997). It should be pointed out that there are large scale descending motions at 500 hPa in part of the western TP and Qaidam Basin as shown in Figure ~~S2~~S3, which lead to less LCC in these regions compared to the other parts of the TP, as shown in Figure 2. In addition, the meteorological stations in the northern ~~part of~~ TP (34-36N, 80-90E) are scarcely and unevenly distributed, and therefore the low LCC in the Taklamakan Desert leads to ~~fake~~ false low LCC values in the northern ~~part of~~ TP (80-90E, 34-36N), as shown in Figure 2. In fact, there are high LCC in these regions as shown in Figure 7 (e).Figure 5 shows the spatial distribution of day time variations of cloud top height in summer. Compared to eastern China at the same latitude, the cloud top height increases significantly from 2:30 pm (~7 km) to 6:30 pm (~14 km) over the TP. The cloud top height approaches the tropopause (~14 km) in the evening, which implies the frequent occurrence of deep convective clouds at this time. This result is consistent with the observation of millimeter-wave radar in Naqu (Yi and Guo, 2016).

By comprehensively analyzing the ~~second Tibet Plateau Experiment (~~TIPEX II~~)~~ sodar data, Xu et al. (2002) and Zhou et al. (2000) found that, with narrow upward motion and time scale from 1.2 h to 1.5 h, the maximum upward motion of the thermal turbulence was identified at the height of about 120 m above the surface, with the vertical speed up to 1 m s^{-1}. They also found symmetrical and wide downward motion areas on either side of the narrow upward motion zone. The question arises as to whether there is a relationship between the formation and evolution of frequent "pop-corn-like" convective clouds and micro-scale thermal turbulence in the atmospheric convective boundary layer over the TP. Xu et al., (2012) speculate these low clouds are probably initiated by strong thermal turbulence under low air density conditions. Compared to the low elevation in eastern China, the increased thermal

turbulence associated with low air density over the TP leads to the different turbulence characteristics of the convective boundary layer (CBL). The CBL is mainly driven by buoyancy heat flux, and the thermal turbulence with organized thermal plume is not totally random (Young, 1988a; Young, 1988b). ~~The BT and ST over the TP are significantly greater than those at the low elevation, which~~The strong BT and ST over the TP play key roles in the convective activities in lower troposphere.

By using the statistical results from sodar data in the ~~second Tibetan Plateau Experiment for atmospheric sciences (~~TIPEX II~~)~~, Zhou et al. (2000) calculated the BT and ST at the height of 50 m under strong convection conditions in Dangxiong (located at central TP). The results indicate that the BT is comparable to ST. Both the thermodynamic and dynamic processes have important influences on the convective activities. Both the BT and ST in the surface layer in Dangxiong are almost an order of magnitude greater than those at low elevation given by Brummer (1985) ~~in~~ over North Sea and Weckwerthet et al. (1997) in Florida. Direct measurements from the Third Tibetan Plateau Experiments (TIPEX III) also confirmed that surface buoyancy flux over the TP is significantly larger than that in eastern China (Zhou, 2000; Wang et al., 2016). Both the sodar data in TIPEX II and boundary layer tower data in TIPEX III showed contributions of BT and ST to the turbulent kinetic energy in the lower troposphere are larger over the TP than over the southeastern margin of the TP and the low-altitude Chengdu Plain (Zhou, 2000; Wang et al., 2015). Thus one might ask the question ~~What~~ what is the relationship between high frequent low cloud and the above physical quantities (e.g. turbulence structure, temperature and humidity) under low air density conditions over the TP? The physical mechanism should be discussed and analyzed. In addition, at low elevation in eastern China, the question arises as to whether or not the variations of PBLH and LCL favor the formation and development of low clouds.

As shown in Figure 6 (a), compared to the low elevation, there is larger LCC (LCC > 50%) over the TP (ASL > 3 km) under low RH_{2m} condition (RH_{2m} < 40%). In contrast, larger LCC mostly corresponds to higher RH_{2m} condition at low elevation, which is consistent~~consisted~~ with our common sense. The above interesting phenomenon can be explained by the differences of PBLH-LCL between the TP and low elevation regions on summer afternoons.~~, which~~ These differences are mainly attributed to following two mechanisms. The first mechanism is that, w~~W~~ith a similar sensible heat flux, the lower air density over the TP leads to greater surface buoyancy flux (or BT) as shown in Figure 6 (c), which is conducive to the increase of PBLH over the TP. Figure 6 (d) shows great ST over the TP, which is mainly attributed to large wind speed. Although here we only show the ST in the surface layer, strong wind shear in the boundary layer probably also plays a role in increasing PBLH over the TP. On the other hand, the second mechanism is that, with a similar RH, Wang et al. (2020) have indicated that, compared to the low elevation in eastern China, the lower temperature over the TP leads to a lower LCL. Together these two mechanisms lead to a greater (PBLH-LCL) difference over the TP on summer afternoons, which increases the probability of air parcels reaching the LCL and forming clouds as shown

in Figure 6 (b). In most cases, the positive value of PBLH-LCL as well as the great BT and ST over the TP corresponds with larger LCC (LCC > 50%) under low RH_{2m} condition (RH_{2m} < 60%), which implies the enhanced local LCC is relevant to the diurnal variation of the PBL process. In contrast, for the eastern China, in most cases, the increased LCC (LCC > 50%) generally corresponds with high RH_{2m} (RH_{2m} > 60%), and the LCC is not significantly correlated with PBLH-LCL or BT and ST, which implies the other factors besides the PBL process (e.g. large scale ascending motion) play a more important in LCC.

13
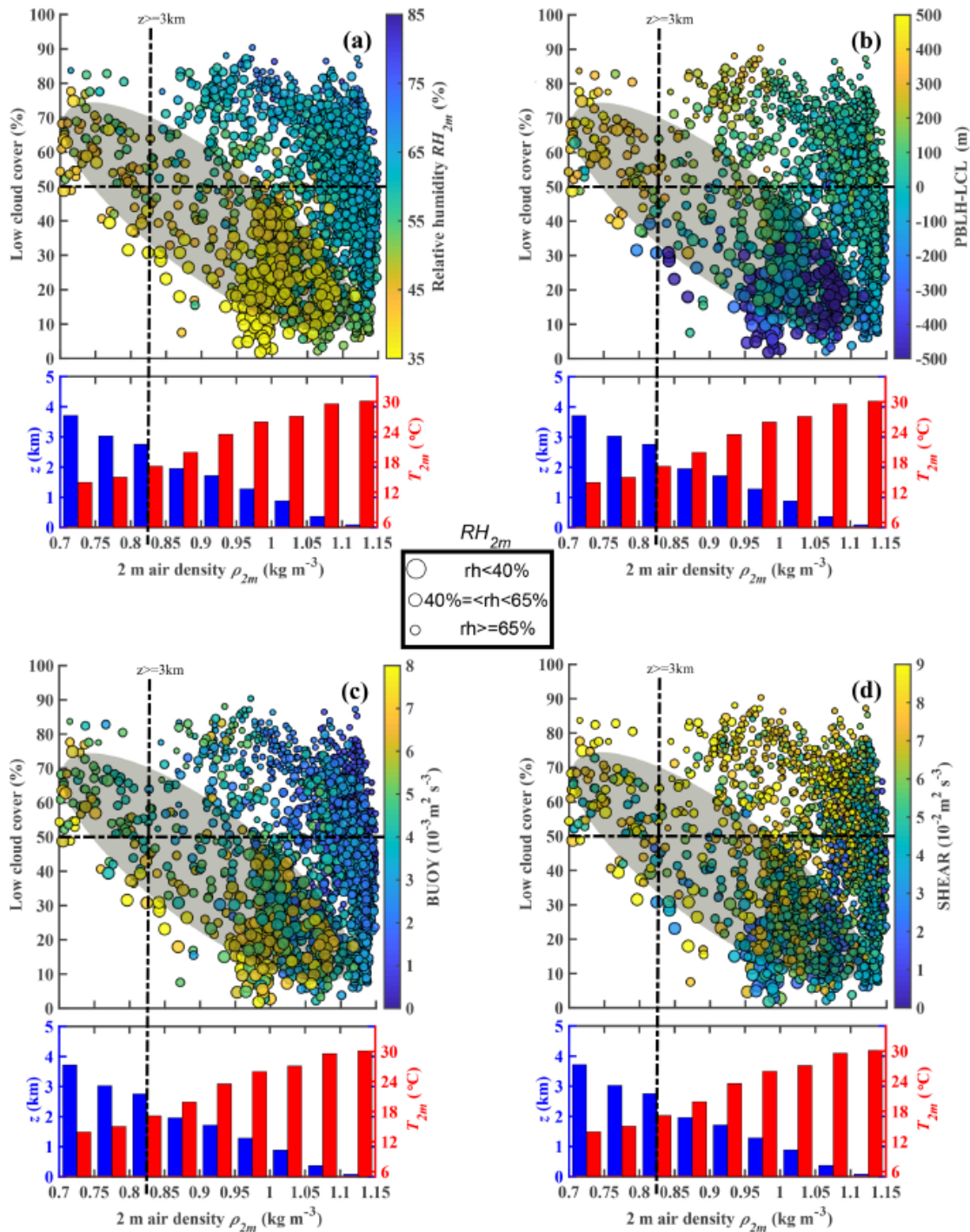
Figure 6. The relationships among monthly means of low cloud cover LCC, ρ_{2m} and (a) RH_{2m}, (b) PBLH-LCL, (c) BT and (d) ST at 2:00 pm Beijing time(BT) from 2010 to 2019 in summer in China. The samples are divided into three groups: RH_{2m} >= 60% (small size dots), 60% > RH_{2m} >= 40% (median size dots) and RH_{2m} < 40% (large size dots). The LCC, T_{2m} and RH_{2m} are observed by in situ measurements, and PBLH, LCL, BT and ST are derived from ERA5 reanalysis data. Here we use the nearest neighbor gridding method to derive PBLH, LCL, BT and ST at each site. The blue and red histograms show the surface elevation z (blue) and air temperature at 2 m (T_{2m}) (red) as functions of 2 m air density (ρ_{2m}). The blue and red histograms show an approximate relationship between ρ_{2m} and surface elevation above sea level z, air temperature at 2 m (T_{2m}) at the bottom of Figure 2a, respectively. The dots with lower RH_{2m} (RH_{2m} < 40%) are mostly distributed within grey shaded elliptic regions as shown in Figure 6 (a)-(d).

Figure 7 (d) shows the mean spatial distribution of PBLH – LCL in the Northern Hemisphere from June to August of 2010-2019. The TP (27-40N, 70-105E) and Rocky Mountains (27-40N, 103-120W) are two typical large topographyhigh value regions in the Northern Hemisphere, and the mean PBLH – LCL over the TP and Rocky Mountains are 376.7 m and -101.9 m, respectively.

Figure 7 (b)-(c) shows the spatial distribution of ST and BT in the Northern Hemisphere from June to August of 2010-2019, respectively. The effect of strong thermal turbulence results in obvious positive values of PBLH – LCL at high elevation regions under low air density conditions in the Northern Hemisphere (BT = 0.008 m^2 s^{-3}, PBLH – LCL = 376.7 m over the TP and BT = 0.011 m^2 s^{-3}, PBLH – LCL = -101.9 m over the Rocky Mountains). Figure 7 (b) also shows that there are strong STs at these two high elevation regions (ST = 0.087 m^2 s^{-3} over the TP and ST = 0.085 m^2 s^{-3} over the Rocky Mountains). Both the BT and ST increase significantly at high elevation due to low air density compared to those at low elevation. The above results enlighten us on thinking about whether the triggering effects of large topography and boundary layer turbulence, which reflect the special turbulence surface characteristics in the boundary layer at high elevation regions under low air density conditions, can be applicable for any large topography in the globe, including TP and other regions (e.g. Rocky Mountains).

Figure 8 shows the a conceptual model of the atmosphere from the near-surface to upper troposphere over the TP. Compared to the low elevation, the TP is characterized by higher PBLH and lower LCL because of strong BT and ST, which is favorable for the formation of shallow clouds in the afternoon. Meanwhile, the large scale ascending motion over the TP results in the transition from shallow clouds to deep convective clouds in the late afternoon and evening.

430
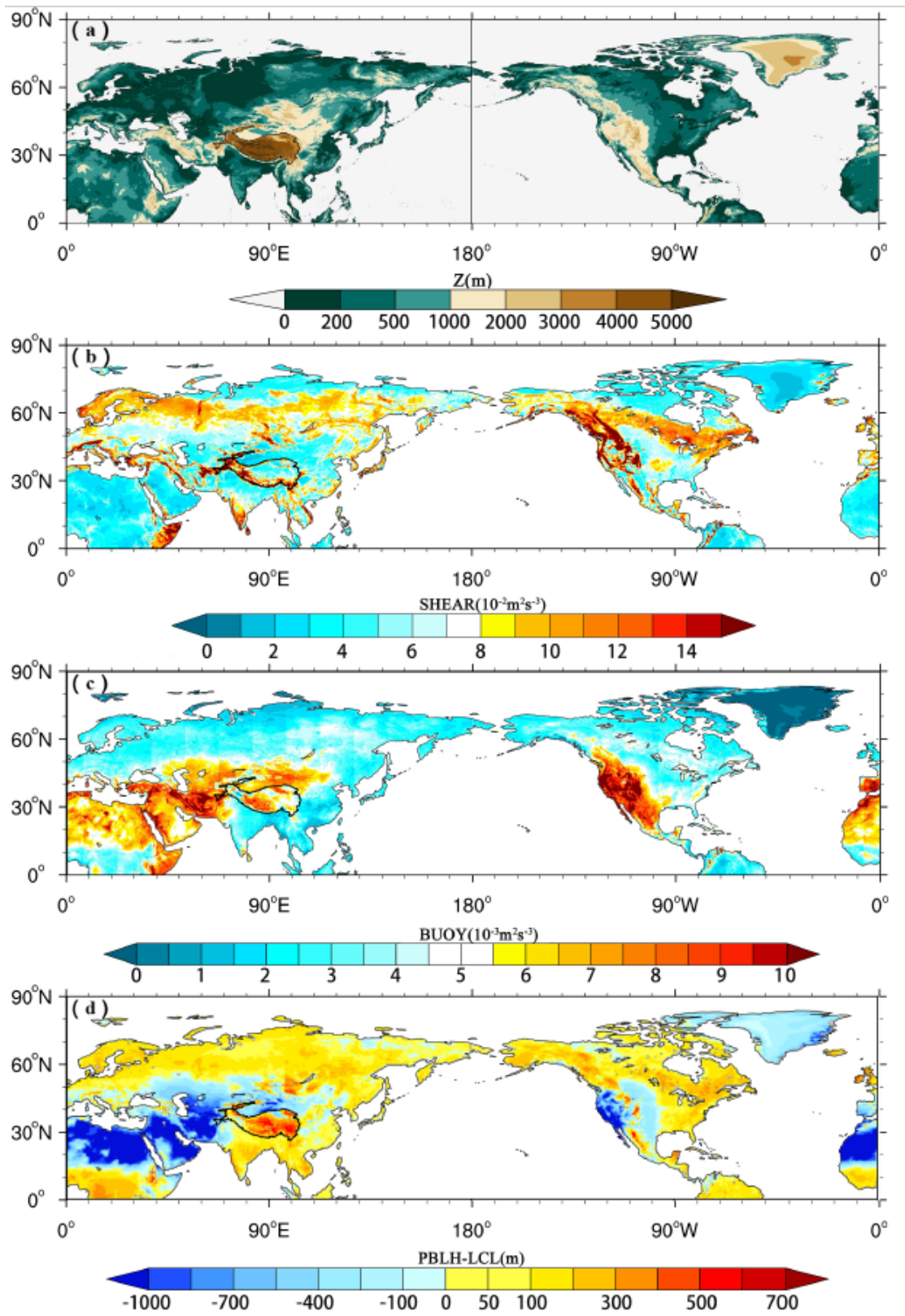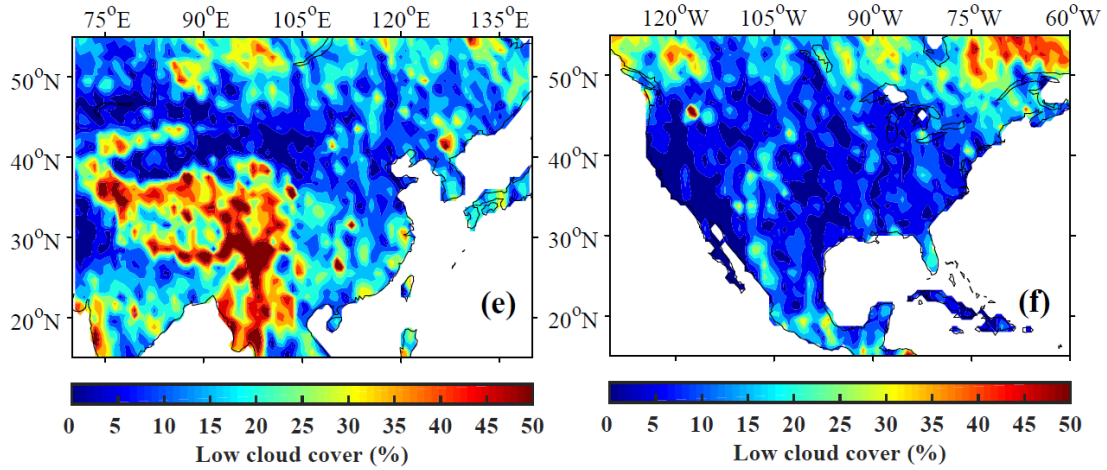
Figure 7. The spatial distribution of (a) ground level elevation (m), (b) ST $(10^{-2}\ m^2\ s^{-3})$, (c) BT $(10^{-3}\ m^2\ s^{-3})$, and (d) PBLH-LCL (m), and (e) LCC derived from ERA5 reanalysis data at local time 2:00 pm in the Northern Hemisphere in summer. Figure (e) and (f) are the summer mean LCC (%) derived from cloudsat satellite data at local time 2:00 pm in eastern China Asia and North America, respectively.
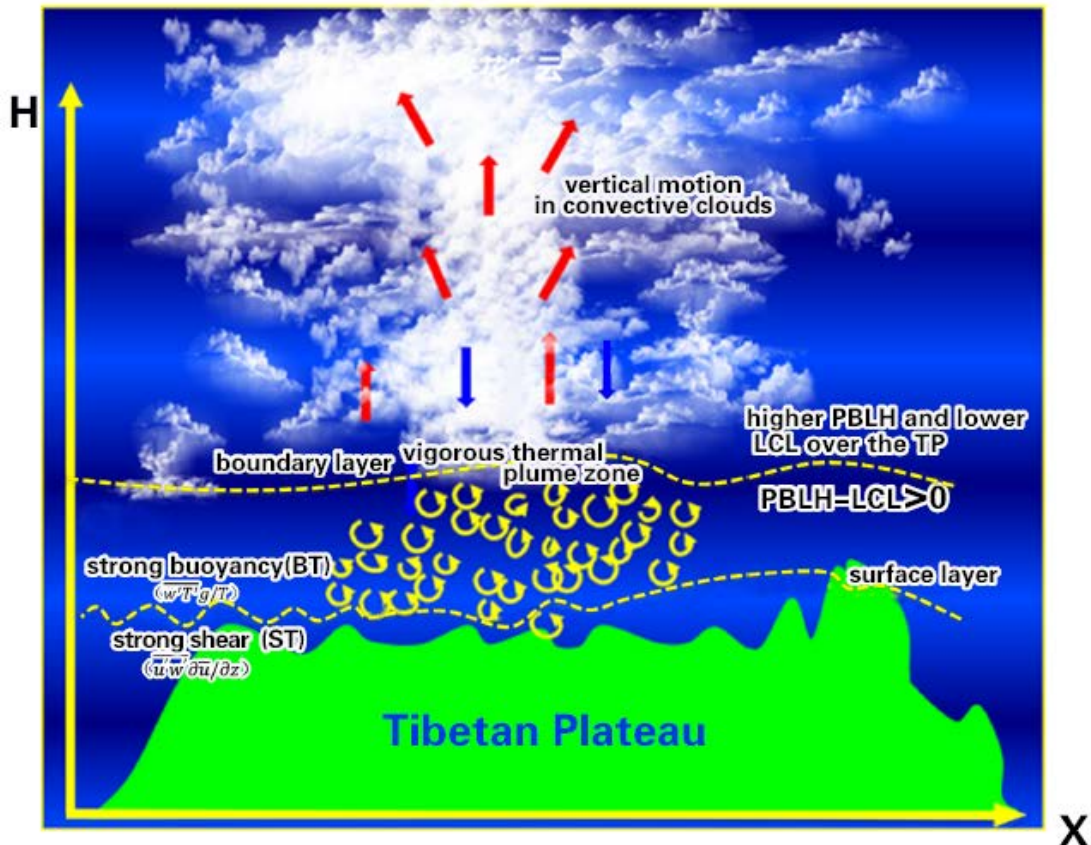
Figure 8. The characteristics model of boundary layer turbulence related to "high efficiency" triggering mechanisms for convection over the TP.

16

4 Conclusions and further discussion

In this study, we focus on the triggering effects of large topography and boundary layer turbulence over the Tibetan Plateau on convection. The topography of the TP also hasplays a major role in the increased occurrences of convective clouds. Our results further confirm the conclusions from Wang et al. (2020), which found that the difference PBLH-LCL in the summer afternoon over the TP is greater than that in eastern China. Compared to the eastern China, with the same relative humidity, lower temperature over the TP results in a lower lifting condensation level. With the same surface sensible heat flux, lower air density over the TP results in a larger buoyancy flux and a deeper boundary layer. The observational results show that, under low relative humidity condition (RH < 40%), the low cloud cover (LCC) is higher than 60% over the TP. In contrast, the high LCC (LCC > 60%) only appears under high RH condition (RH > 60%) at low elevation.

In general, LCC increases with the increasing elevation. The median of LCCs at high elevation (TP) is significantly greater than those at low elevation (eastern China) throughout the day. The diurnal variations of LCC at low elevationin eastern China are generally distributed in an unimodal pattern with the maximum appearing at 2:00 pm Beijing timeBT and low values during the night. The diurnal variations of LCC at high elevation (TP) present a bimodal curve with the maximum appearing at 5:00 pm Beijing timeBT and the secondary local maximum appearing at 8:00 am Beijing timeBT. In addition, LCC maintains at high values at high elevation (TP) during the day. The median cloud top height derived from himawariHimawari-8 retrieval product shows the transition from shallow clouds to deep convective clouds in the late afternoon and evening over the TP, which is attributed to the strong large-scale ascending motion from the near surface to upper troposphere over the TP.

The buoyancy term (BT) and shear term (ST) over the TP are significantly greater than those at the low elevation, which is favorable for the increasing of PBLH. Similar phenomenaon occurs at other high elevation areas (e.g. Rocky Mountains). The strong thermal turbulence and large scale ascending motion jointly results in positive value of PBLH-LCL at high elevation regions under low RH condition over the TPin the Northern Hemisphere. The slightly greater than zero PBLH-LCL corresponds spatially to increased LCC in the central part of Rocky Mountains, but t The obvious large-scale subsidence on both sides of the Rocky mountain Mountain especially the western side leads to strong inversion above PBL and lower RH within the PBL, which further lead to negative value of PBLH-LCL and decreased LCC in most part of Rocky Mountainthese areas. The slightly greater than zero PBLH-LCL corresponds spatially to increased LCC in the partial regions of central Rocky Mountain. Thus less LCC is generated at the Rocky Mountains compared to the TP.

Data availability

All reanalysis data used in this study were obtained from publicly available sources: ERA5 reanalysis data can be obtained from the ECMWF public datasets web interface

(http://apps.ecmwf.int/datasets/). The satellite (CloudSat radar and Calipso lidar)-merged cloud classification product 2B-CLDCLASS-lidar were obtained from Colorado State University (http://www.cloudsat.cira.colostate.edu/data-products/level-2b/2b-cldclass-lidar). The ~~himawari~~Himawari-8 retrieval products were obtained from JAXA Himawari Monitor (https://www.eorc.jaxa.jp/ptree/).

Code Availability

The data in this study are analysed with MATLAB and NCL. Contact Y.W. for specific

code requests.

Author Contributions

X.X. and Y. W. led this work with contributions from all authors. Y.T. and Y. W. made the calculations and created the figures. X.X., Y.W., H.Z. and M.Z. led analyses, interpreted results and wrote the paper. R.L. supports high resolution satellite Gaofen images to show the organized structures (cellular convection) for shallow convection.

Competing interests

The authors declare no competing interests.

References

Brümmer, B.: Structure, dynamics and energetics of boundary layer rolls from Kon Tur aircraft observations, undefined, 1985.

Dyer, A. J.: A review of flux-profile relationships, Bound.-Layer Meteorol., 7, 363–372, https://doi.org/10.1007/bf00240838, 1974.

Ek, M. and Mahrt, L.: Daytime Evolution of Relative Humidity at the Boundary Layer Top, Mon. Weather Rev., 122, 2709–2721, https://doi.org/10.1175/1520-0493(1994)122<2709:DEORHA>2.0.CO;2, 1994.

Findell, K. L. and Eltahir, E. A. B.: Atmospheric Controls on Soil Moisture–Boundary Layer Interactions. Part I: Framework Development, J. Hydrometeorol., 4, 552–569, https://doi.org/10.1175/1525-7541(2003)004<0552:ACOSML>2.0.CO;2, 2003.

Flohn, H. and Reiter, E. R.: Contributions to a meteorology of the Tibetan highlands, 1967.

Holtslag, A. A. M. and De, Bruin, H. A. R.: Applied modelling of the night time surface energy balance over land. J. Appl. Meteorol., 27, 689–704. doi: 10.1175/1520-0450(1988)027<0689:AMOTNS>2.0.CO;2, 1988.

Gentine, P., Holtslag, A. A. M., D'Andrea, F., and Ek, M.: Surface and Atmospheric Controls on the Onset of Moist Convection over Land, J. Hydrometeorol., 14, 1443–1462, https://doi.org/10.1175/JHM-D-12-0137.1, 2013.

Gryanik, V. M., Lüpkes, C., Grachev, A., & Sidorenko, D.: New modified and extended stability functions for the stable boundary layer based on SHEBA and parametrizations of bulk transfer coefficients for climate models. J. Atmos. Sci., 77(8), 2687-2716, https://doi.org/10.1175/JAS-D-19-0255.1, 2020.

Guillod, B. P., Orlowsky, B., Miralles, D. G., Teuling, A. J., and Seneviratne, S. I.: Reconciling spatial and temporal soil moisture effects on afternoon rainfall, Nat. Commun., 6, 6443, https://doi.org/10.1038/ncomms7443, 2015.

Hersbach, H., Bell, B., Berrisford, P., Hirahara, S., Horányi, A., Muñoz-Sabater, J., Nicolas, J., Peubey, C., Radu, R., Schepers, D., Simmons, A., Soci, C., Abdalla, S., Abellan, X., Balsamo, G., Bechtold, P., Biavati, G., Bidlot, J., Bonavita, M., Chiara, G. D., Dahlgren, P., Dee, D., Diamantakis, M., Dragani, R., Flemming, J., Forbes, R., Fuentes, M., Geer, A., Haimberger, L., Healy, S., Hogan, R. J., Hólm, E., Janisková, M., Keeley, S., Laloyaux, P., Lopez, P., Lupu, C., Radnoti, G., Rosnay, P. de, Rozum, I., Vamborg, F., Villaume, S., and Thépaut, J.-N.: The ERA5 global reanalysis, Q. J. R. Meteorol. Soc., 146, 1999–2049, https://doi.org/10.1002/qj.3803, 2020.

Li, Y. and Zhang, M.: Cumulus over the Tibetan Plateau in the Summer Based on CloudSat–CALIPSO Data, J. Clim., 29, 1219–1230, https://doi.org/10.1175/JCLI-D-15-0492.1, 2016.

Luo, Y., Zhang, R., Qian, W., Luo, Z., and Hu, X.: Intercomparison of Deep Convection over the Tibetan Plateau–Asian Monsoon Region and Subtropical North America in Boreal Summer Using CloudSat/CALIPSO Data, J. Clim., 24, 2164–2177, https://doi.org/10.1175/2010JCLI4032.1, 2011.

Romps, D. M. (2017). Exact expression for the lifting condensation level. Journal of the Atmospheric Sciences, 74, 3891–3900. https://doi.org/10.1175/JAS‐D‐17‐0102.1

Sassen, K. and Wang, Z.: Classifying clouds around the globe with the CloudSat radar: 1-year of results, Geophys. Res. Lett., 35, https://doi.org/10.1029/2007GL032591, 2008.

Smith, R. K.: On the theory of CISK, Q. J. R. Meteorol. Soc., 123, 407–418, 1997.

Stull, R. B.: Mean Boundary Layer Characteristics, in: An Introduction to Boundary Layer Meteorology, edited by: Stull, R. B., Springer Netherlands, Dordrecht, 1–27,

https://doi.org/10.1007/978-94-009-3027-8_1, 1988.

Sugimoto, S. and Ueno, K.: Role of Mesoscale Convective Systems Developed around the Eastern Tibetan Plateau in the Eastward Expansion of an Upper Tropospheric High during the Monsoon Season, J. Meteorol. Soc. Jpn. Ser II, 90, 297–310, https://doi.org/10.2151/jmsj.2012-209, 2012.

Taylor, C. M., de Jeu, R. A. M., Guichard, F., Harris, P. P., and Dorigo, W. A.: Afternoon rain more likely over drier soils, Nature, 489, 423–426, https://doi.org/10.1038/nature11377, 2012.

Tuttle, S. and Salvucci, G.: Empirical evidence of contrasting soil moisture–precipitation feedbacks across the United States, Science, 352, 825–828, https://doi.org/10.1126/science.aaa7185, 2016.

Wang, Y., Xu, X., Zhao, T., Sun, J., Yao, W., and Zhou, M.: Structures of convection and turbulent kinetic energy in boundary layer over the southeastern edge of the Tibetan Plateau, Sci. China Earth Sci., 58, 1198–1209, https://doi.org/10.1007/s11430-015-5054-1, 2015.

Wang, Y., Xu, X., Liu, H., Li, Y., Li, Y., Hu, Z., Gao, X., Ma, Y., Sun, J., Lenschow, D. H., Zhong, S., Zhou, M., Bian, X., and Zhao, P.: Analysis of land surface parameters and turbulence characteristics over the Tibetan Plateau and surrounding region, J. Geophys. Res. Atmospheres, 121, 9540–9560, https://doi.org/10.1002/2016JD025401, 2016.

Wang, Y., Zeng, X., Xu, X., Welty, J., Lenschow, D. H., Zhou, M., and Zhao, Y.: Why Are There More Summer Afternoon Low Clouds Over the Tibetan Plateau Compared to Eastern China?, Geophys. Res. Lett., 47, e2020GL089665, https://doi.org/10.1029/2020GL089665, 2020.

Weckwerth, T. M., Wilson, J., Wakimoto, R., and Crook, N. A.: Horizontal convective rolls: Determining the environmental conditions supporting their existence and characteristics, Mon. Weather Rev., 125, 505–526, https://doi.org/10.1175/1520-0493(1997)12560;0505:hcrdte62;2.0.co;2, 1997.

Wu, G., Duan, A., Liu, Y., Mao, J., Ren, R., Bao, Q., He, B., Liu, B., and Hu, W.: Tibetan Plateau climate dynamics: recent research progress and outlook, Natl. Sci. Rev., 2, 100–116, https://doi.org/10.1093/nsr/nwu045, 2015.

Xu, X., Zhou, M., Chen, J., Bian, L., Zhang, G., Liu, H., Li, S., Zhang, H., Zhao, Y., Suolongduoji, and Jizhi, W.: A comprehensive physical pattern of land-air dynamic and thermal structure on the Qinghai-Xizang Plateau, Sci. China Ser. D, 45, 577–594, https://doi.org/10.1360/02yd9060, 2002.

Xu, X., Zhang, R., Koike, T., Lu, C., Shi, X., Zhang, S., Bian, L., Cheng, X., Li, P., and Ding, G.: A New Integrated Observational System Over the Tibetan Plateau, Bull.

Am. Meteorol. Soc. - BULL AMER METEOROL SOC, 89, 1492–1496, https://doi.org/10.1175/2008BAMS2557.1, 2008.

Xu, X., Shi, X., and Lu, C.: Theory and application for warning and prediction of disastrous weather downstream from the Tibetan Plateau, Theory Appl. Warn. Predict. Disastrous Weather Downstr. Tibet. Plateau, 1–116, 2012.

Xu, X., Zhao, T., Lu, C., Guo, Y., Chen, B., Liu, R., Li, Y., and Shi, X.: An important mechanism sustaining the atmospheric "water tower" over the Tibetan Plateau, Atmospheric Chem. Phys., 14, 11287–11295, https://doi.org/10.5194/acp-14-11287-2014, 2014.

Yi, C., and Guo, X.: Characteristics of convective cloud and precipitation during summer time at Naqu over Tibetan Plateau (in Chinese), Chinese Science Bulletin, 61, 1706–471, https://doi.org/10.1360/N972015-01292, 2016.

Young, G. S.: Convection in the atmospheric boundary layer, Earth-Sci. Rev., 25, 179–198, https://doi.org/10.1016/0012-8252(88)90020-7, 1988a.

Young, G. S.: Turbulence Structure of the Convective Boundary Layer. Part I. Variability of Normalized Turbulence Statistics, J. Atmospheric Sci., 45, 719–726, https://doi.org/10.1175/1520-0469(1988)045<0719:TSOTCB>2.0.CO;2, 1988b.

Zhou, M., Xu, X., Bian, L., Chen, J., Liu H., Zhang, H., Li, S., and Zhao J.: Observational analysis and dynamic study of atmospheric boundary layer on Tibetan Plateau (in Chinese), 125 pp., 2000.